nature geoscience

ARTICLES

https://doi.org/10.1038/s41561-021-00802-4

Transient ocean oxygenation at end-Permian mass extinction onset shown by thallium isotopes

Sean M. Newby[1]✉, Jeremy D. Owens[1], Shane D. Schoepfer[2] and Thomas J. Algeo[3]

The end-Permian mass extinction (EPME) represents the largest biocrisis in Earth's history, a result of environmental perturbations following volatiles released during Siberian Traps magmatism. A leading hypothesis links the marine mass extinction to the expansion of oceanic anoxia, although uncertainties exist as to the timing and extent. Thallium isotopes, a novel palaeoredox proxy with a rapid global response due to its short residence time in seawater, track global rates of manganese oxide burial, one of the first redox half-reactions to occur under reduced oxygen conditions. For this study, we analysed thallium isotopes from three widely distributed sites in Panthalassa, the largest ocean basin at the time. Our results provide evidence for the onset of deoxygenation considerably before the EPME, earlier by ≥1 Myr than the onset implied by other proxy records. Notably, there is a transient negative thallium isotope excursion concurrent with the EPME, which requires substantial manganese oxide burial based on the thallium isotope mass balance. This feature suggests a brief oxygenation episode before a return to more anoxic conditions, implying a more complex redox scenario, with rapid changes in oceanic (de)oxygenation leading to spatially and temporally variable biotic stresses. This oxygenation event may have been related to a transient cooling episode, based on published oxygen isotope records. These findings show that the Earth system experienced a highly fluctuating response to forcings linked to volcanogenic volatiles during the EPME.

The end of the Palaeozoic Era was marked by the largest mass extinction of the Phanerozoic Eon, the end-Permian mass extinction (EPME). This event, immediately preceding the Permian/Triassic boundary (PTB, ~252 million years ago (Ma)), was characterized by the loss of ~90% of all marine species[1–3]. Identifying the environmental conditions and mechanisms underlying this major biocrisis is important for understanding the Earth-system feedbacks that operated during this event. The primary extinction mechanism is hypothesized to have been emplacement of the Siberian Traps large igneous province (LIP)[1,4–8], releasing volatiles such as CO_2, CH_4 and SO_2 (refs. [5,7,9]), which led to a cascade of detrimental environmental effects[4,6–8]. These effects include short-term cooling[9,10], long-term warming[8–13], ocean acidification[14,15], acid rain[16], oceanic anoxia[17–22], widespread euxinia (anoxic and sulfidic water column)[17,18,20,23,24], heavy metal toxicity[25] and ozone depletion[7,26].

Recent studies suggest that major fluctuations in global temperatures occurred during the EPME, most notably a hyperwarming driven by volcanogenic greenhouse gases[5,9,10,12,13], which caused a variety of environmental responses at different timescales[6,8]. Marine faunas suffered from the direct effects of global warming[6,11] and from more indirect effects of high temperature, which included increased weathering[8,19,27], enhanced marine primary productivity from riverine nutrient fluxes[27], slowed thermohaline circulation due to a reduced meridional temperature gradient[9,19,21,22], and decreased gas solubility[9,22]; these effects likely led to large-scale disruption of the marine food web[8,28]. In addition, short-term cooling may have occurred via increased volcanic SO_2 emissions[5,9].

Expansion of oceanic anoxia due to several warming-related effects[8,9,19,22] was likely an important mechanism driving the marine mass extinction[4,6,8,17,18,21–23]. A shift towards more reducing conditions at the EPME has been inferred in multiple oceanic regions based on biomarkers[23], trace-metal concentrations[18,19], pyrite framboid size distributions[17,18] and iron speciation data[20,23], as well as the global ocean uranium isotope proxy[21,29]. However, most geochemical redox proxies have modern seawater residence times that are either too short relative to oceanic mixing time (~1–2 kyr) to record global changes (for example, ~100 yr for Fe)[20,23], or too long to capture rapid shifts in oceanic redox conditions (for example, ~400 kyr for Mo or U)[29,30]. Furthermore, most of these proxies are activated at relatively low redox potentials[31,32], limiting their ability to capture the initial onset of gradual deoxygenation events.

The use of thallium isotopes as a palaeoredox proxy is new[33–35], but the global Tl isotope mass balance framework is well established[32]. Importantly, Tl isotopes have the potential to track global rates of manganese oxide reduction and burial[31,32], which is one of the first redox half-reactions following oxygen depletion on the redox ladder[32,36]. In well-oxygenated marine systems, Mn(IV) forms Mn oxides that are readily buried in sediments[36]. Under anoxic conditions, Mn oxides are rapidly remineralized, releasing dissolved Mn^{2+} back to the water column[36]. As Mn reduction potential is only slightly less than that of oxygen but greater than that of nearly all other redox-sensitive elements[32,36], it is one of the first elements to respond to changes in (de)oxygenation, making the Mn cycle highly sensitive to redox variation. However, tracking the global Mn cycle in the sedimentary record is difficult[31] because Mn has an extremely short modern oceanic residence time (~60 yr) and has only a single long-lived stable isotope (^{55}Mn)[32].

Recent work has shown that the Tl isotopic composition of seawater is largely controlled by the global Mn oxide burial flux at short timescales (that is, less than a few million years)[31–35]. With a seawater residence time of 18.5 kyr, Tl is globally well mixed but still responds rapidly (from a stratigraphic perspective) to changes in

[1]Earth, Ocean, and Atmospheric Science Department, National High Magnetic Field Laboratory, Florida State University, Tallahassee, FL, USA. [2]Department of Geosciences and Natural Resources, Western Carolina University, Cullowhee, NC, USA. [3]Department of Geology, University of Cincinnati, Cincinnati, OH, USA. ✉e-mail: smn17b@my.fsu.edu

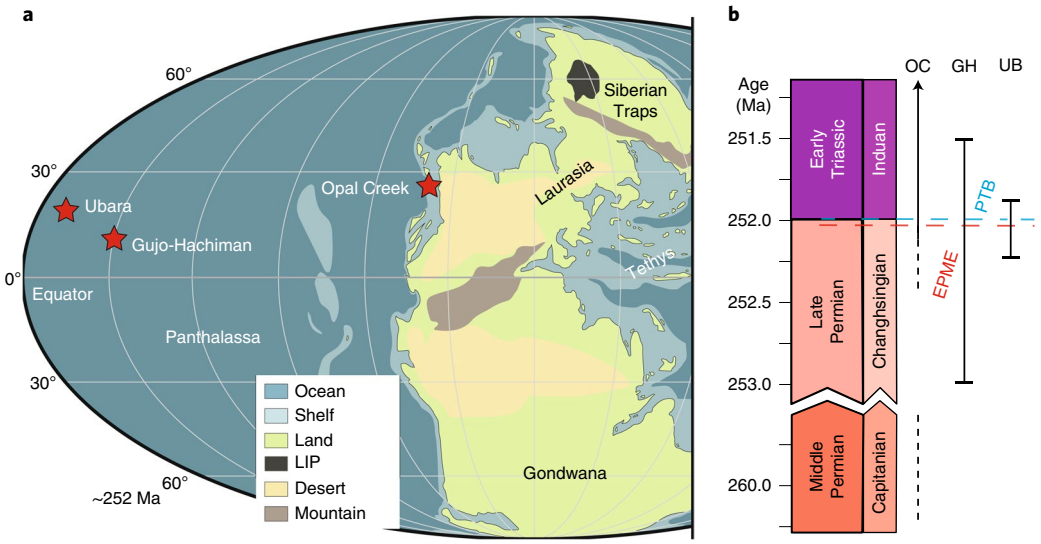

Fig. 1 | Site locations during the EPME. a, Location of the three study sections in the Late Permian to Early Triassic (~252 Ma). Major landmasses and oceans are labelled, as well as the location of the Siberian Traps (modified from ref. [50]). **b**, Approximate correlation of the stratigraphic intervals of the three study sections, including Opal Creek (OC) from Middle Permian to Lower Triassic with Upper Permian unconformity[40], Gujo-Hachiman (GH) representing ~1.5 Myr across the EPME and PTB[18] and Ubara (UB) representing only ~0.3 Myr within the interval represented by Gujo-Hachiman[18].

marine oxygenation[31,32]. Thallium isotopic compositions are compared to the NIST 997 thallium metal standard and reported as:

$$\varepsilon^{205}\mathrm{Tl} = \left(^{205}\mathrm{Tl}/^{203}\mathrm{Tl}_{\mathrm{sample}} - {}^{205}\mathrm{Tl}/^{203}\mathrm{Tl}_{\mathrm{NIST\ 997}}\right) / \left(^{205}\mathrm{Tl}/^{203}\mathrm{Tl}_{\mathrm{NIST\ 997}}\right) \times 10{,}000.$$

The modern seawater Tl isotope composition ($\varepsilon^{205}\mathrm{Tl}_{sw}$) is ~−6.0 (refs. [32,37] and references therein), with no major isotopic variation beyond analytical error. With little average isotopic variation in the sources of Tl to the ocean (all near $\varepsilon^{205}\mathrm{Tl}$ ~−2.0) (ref. [37] and references therein), changes in source fluxes, including weathering mechanisms, have minor isotopic leverage on the marine reservoir. Thus, changes in Tl sinks are the primary driver of secular variation in $\varepsilon^{205}\mathrm{Tl}_{sw}$. One major sink is adsorption of Tl onto the low-temperature Mn oxide birnessite (estimated at ~32% of total Tl burial from observations and isotopic mass balance), a process that yields the largest known Tl isotopic fractionation from seawater (+16.0 ε units) (refs. [32,37] and references therein). The second major sink is low-temperature alteration of oceanic crust (AOC, estimated at ~63% of total Tl burial), which imparts a smaller negative isotopic fractionation from seawater (−1.2 ε units) (ref. [37] and references therein). Critically, only Mn oxide perturbations are implicated for short-term climatic events because changes in AOC require multi-million-year timescales and have limited isotopic leverage[31]. Thus, AOC is not considered as a potential driver of the Tl isotopic fluctuations in the present study sections given the short timescale and large magnitude of the observed perturbations. A minor sink is Tl adsorption by syngenetic pyrite in the water column or diagenetic pyrite in anoxic to sulfidic sediments (~4% of total Tl burial)[32]. With no isotopic fractionation[31], this sink provides a mechanism to faithfully capture the global $\varepsilon^{205}\mathrm{Tl}_{sw}$ value[31,32,38]. Therefore, analysis of the $\varepsilon^{205}\mathrm{Tl}$ of sedimentary pyrites has the potential to provide a more detailed and nuanced understanding of changes in ocean redox conditions in relation to the timing and pace of the EPME.

Warming and anoxia before EPME

Thallium isotopes from three widely separated Panthalassic sections (Fig. 1) were analysed. Both the Gujo-Hachiman and Ubara sections in Japan represent abyssal settings at peri-equatorial latitudes during the Permian–Triassic transition[18,39]. These sections have been dated based on radiolarian biostratigraphy and carbon isotopic chemostratigraphy, and tentatively correlated with shallow-marine Tethyan carbonate sections, which employ conodont biostratigraphy[18,39]. The third study section at Opal Creek, Alberta, Canada represents a mid-latitude deep-shelf setting that has been dated using conodonts and carbon isotopic chemostratigraphy[19,40]. It consists of a thin Middle Permian unit unconformably overlain by stratigraphically condensed uppermost Permian beds (including the EPME interval) and a relatively thick Lower Triassic succession[19,40] (Fig. 1). Importantly, these sites all record local anoxic to euxinic conditions based on previous trace-metal studies[18,19] (Extended Data Fig. 1 and Supplementary Data), thus having the potential to record the global Tl isotope seawater value in pyrite[31].

An unconformity in the Opal Creek section limits analysis of geochemical changes in the Upper Permian, but the section does provide a record from the underlying Middle Permian. Beds near the base of the section dated to the Capitanian (265 to 259 Ma)[40] have $\varepsilon^{205}\mathrm{Tl}$ values ~−6.5 (Fig. 2a), within the range of modern oxic seawater values. This suggests that Mn oxide burial rates were roughly similar to the modern rates, and indicates that seawater redox conditions were predominantly oxic (Fig. 3a), provided that other fluxes (for example, AOC) had near-modern values[32,41,42].

The Gujo-Hachiman section yields Changhsingian (254–252 Ma) $\varepsilon^{205}\mathrm{Tl}$ values of ~−4.0 (Fig. 2b), which are slightly more positive than the older values from Opal Creek and indicate a decrease in the Mn oxide burial flux from the Capitanian to the Changhsingian. The reduction of Mn oxide burial suggests an expansion of seafloor anoxia by at least 1.0 Myr (based on a published astrochronological age model[18]) prior to the redox shift recorded by $\delta^{238}\mathrm{U}$ near the EPME horizon[21,29], and possibly even earlier due to the large stratigraphic gap at Opal Creek (the entire Wuchiapingian stage, ≥5 Myr). From the base of the Gujo-Hachiman section to 685 cm, the $\varepsilon^{205}\mathrm{Tl}$ profile exhibits a trend to more positive values, reaching −2.0 just before the EPME (Fig. 2b).

A similar pattern is observed in the Ubara section despite its greater stratigraphic condensation[18], in which an $\varepsilon^{205}\mathrm{Tl}$ of ~−2.0 was maintained from the base of the section (roughly correlative to ~500 cm at Gujo-Hachiman) to 90 cm (Fig. 2c). These values suggest that there was limited global burial of Mn oxides due to widespread

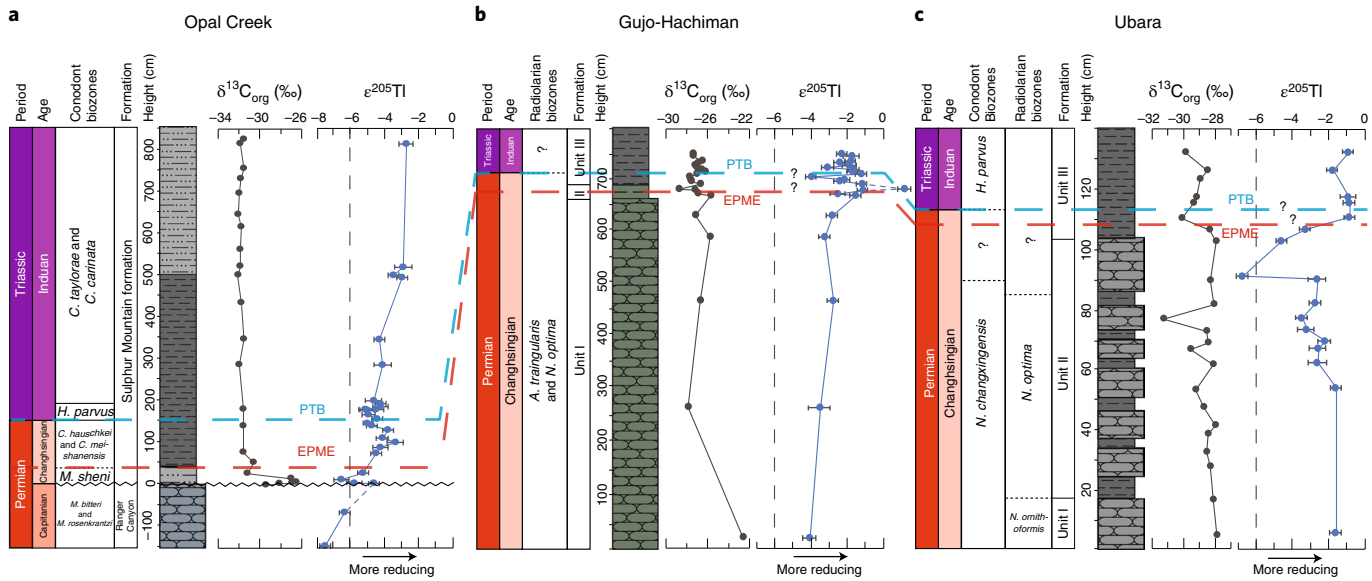

Fig. 2 | Thallium isotope stratigraphy of each section. a–c, Biostratigraphy, lithostratigraphy and chemostratigraphy for Opal Creek (**a**), Gujo-Hachiman (**b**) and Ubara (**c**), including organic carbon ($\delta^{13}C_{org}$, black line) and thallium ($\varepsilon^{205}Tl$, blue line) isotopes. Biostratigraphy and lithostratigraphy are from previous sources[18,19,39,40], as are those of the carbon isotopes of Opal Creek[40]. Lithostratigraphic columns are present in the centre adjacent to height. Separate patterns are used to distinguish lithologies, including chert (rounded bricks), shale (dashed lines) and silty mudstones (dashed and dotted lines), with approximate colour of the rocks. The Tl isotope plots have a dashed vertical line indicating modern seawater values, with more positive values representing a greater extent of anoxia. All three sites are correlated with the EPME (red dashed line) and PTB (blue dashed line) using both biostratigraphy and carbon isotope chemostratigraphy. Thallium isotopes are plotted with error bars (2σ). All carbon isotope errors are smaller than the symbol (2σ < ±0.4‰). Opal Creek features an Upper Permian unconformity near the base of the described section (wavy line), below the EPME[19,40].

oceanic anoxia during the latest Permian. Thus, globally extensive deoxygenation occurred well before the EPME (Fig. 3b) and was possibly related to early marine ecosystem deterioration[43].

The observed temporal offset between shifts in $\varepsilon^{205}Tl$ compared to those of $\delta^{238}U$ (Fig. 4) are not likely to be explained by differences in oceanic residence times and was most likely due to the sensitivity of $\varepsilon^{205}Tl$ to changes in rates of Mn oxide reduction[31,32], whereas $\delta^{238}U$ responds to changes in Fe oxide reduction[29,32]. This suggests that average global ocean redox conditions were closer to the Mn(IV)–Mn(III) threshold than to that of Fe(III)–Fe(II) for much of the Changhsingian. A similar high sensitivity of the Tl isotope proxy has been reported for other major Phanerozoic oceanic anoxic events (OAEs)[33–35]. The Changhsingian at Gujo-Hachiman is not characterized by a positive shift in carbonate carbon isotopes[11,39,44], providing no indirect geochemical evidence for an increase in global organic carbon burial preceding the EPME. Although increased organic carbon burial is a recognized feature of many Phanerozoic OAEs[33–35], such a record may have been obscured by inputs of isotopically light carbon from volcanic sources or weathering of organic carbon[5]. In addition, the expansion of oceanic anoxia during the pre-EPME Changhsingian may have been due to some mechanism other than organic matter burial (for example, climatic warming[10,12,13], inducing slowed global ocean circulation and reduced oxygen solubility in seawater[9,22]). Body size decreases and morphological simplification among ammonoids and possibly other marine clades[15,43] during the Changhsingian may have been driven by the limited shift towards more reducing conditions indicated by this Tl isotope record, which coincided with high-latitude environmental deterioration[15] and temperature increases[12,13] and overlapped with early intrusive activity of the Siberian Traps LIP[5].

Rapid redox changes during EPME

The most striking feature observed in all three study sections is a large negative $\varepsilon^{205}Tl$ excursion near the EPME. At Ubara, $\varepsilon^{205}Tl$ shifts from −2.0 at 90 cm to −6.5 at 92 cm and then returns to −1.0 by 110 cm and stabilizes (Fig. 2c). At Gujo-Hachiman, $\varepsilon^{205}Tl$ is −2.0 at 715 cm, declines to −4.0 at 720 cm and then returns to −2.0 by 725 cm and stabilizes (Fig. 2b). At Opal Creek, a negative excursion is observed just prior to the EPME. However, its exact stratigraphic range is somewhat uncertain due to the Upper Permian unconformity possibly truncating the beginning of this excursion and due to a condensing of the latest Permian beds[40]. There, $\varepsilon^{205}Tl$ is −4.5 immediately above the unconformity (~0 cm), becomes highly negative (−6.5) at 10 cm and then returns to −5.0 at 25 cm (Fig. 2a). Above 40 cm at Opal Creek, $\varepsilon^{205}Tl$ shifts rapidly to more positive values (−4.0) by 80 cm, trends to −2.0 by 500 cm (Fig. 2a) and stabilizes near this value for the next ~40 m of the Lower Triassic (Extended Data Fig. 1).

The brief negative $\varepsilon^{205}Tl$ excursion in the uppermost Permian and the subsequent long-term positive trend through the lowermost Triassic imply large and rapid oceanic redox fluctuations around the EPME. These redox fluctuations likely intensified stresses on marine organisms, especially given an estimated duration for the negative excursion of just ~60 kyr (based on published astrochronological age models for the Japanese sections[18]; see Supplementary Discussion). The negative Tl excursion provides evidence of a transient increase in Mn oxide burial at the onset of the EPME, as no other process (including diagenesis) is known to be capable of generating a large-magnitude excursion at such a short timescale[31,32]. Such a negative seawater Tl isotope excursion has not previously been documented for any other Phanerozoic OAE[33–35], nor has such a redox change been inferred from other palaeoredox records for the EPME[18,19,21,29], possibly due to differences in their sensitivity to Mn oxide burial and/or their seawater residence times[31,32].

Although an $\varepsilon^{205}Tl_{sw}$ value of ~−6 during the EPME excursion indicates an expansion of oxic seafloor and is similar to the modern seawater value, it may not directly compare. The modern global marine burial flux of Mn oxides is Mn-limited. Consequently, the

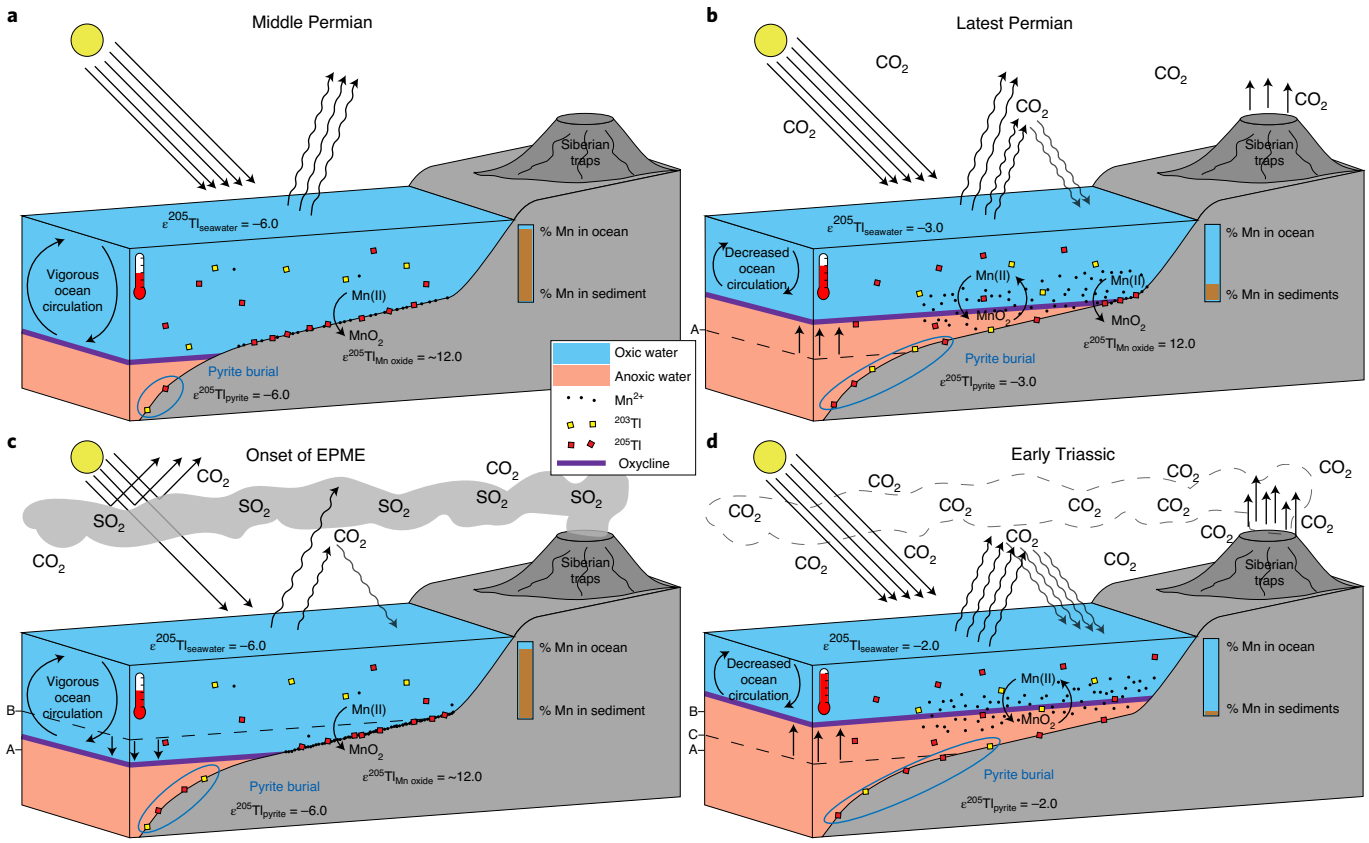

Fig. 3 | Model of Permian–Triassic oceanic redox changes as related to thallium isotopes. a–d, Changes in oceanic redox conditions, the Mn cycle, and their effects on the ε^{205}Tl of multiple reservoirs. Note that all features and values are representational and approximate (for example, temperature based on fill of thermometer). Changes in the oxycline are shown on the left side of panels using tick marks labelled A, B and C. The Middle Permian (**a**) had oceanographic dynamics and chemical signatures similar to modern conditions. Before the EPME during the latest Permian (**b**), there were increased temperatures, expansion of marine anoxia leading to elevated dissolved Mn^{2+}, and less fractionated Tl isotopes. At the onset of the EPME (**c**), short-term cooling due to increased SO_2 emissions led to geochemical signals similar to those of the Middle Permian. Following the onset of the EPME and into the Early Triassic (**d**), there was a return to the reducing conditions of before the EPME (**b**), but these conditions were spatially more extensive.

modern seawater Tl isotopic value is largely controlled by the availability of Mn, not the extent of oxic seafloor. During the EPME, the dissolved marine Mn reservoir may have been larger due to earlier remineralization of Mn oxides related to extensive oceanic anoxia (that is, decreased burial interpreted from higher ε^{205}Tl; Fig. 3b) and/or increased Mn delivery related to enhanced continental weathering[19,27]. However, enhanced weathering could not have driven the ε^{205}Tl signal on its own; the observed fractionation requires Mn oxide burial, which implies that the ocean became more oxygenated during the latest Changhsingian as the values of ε^{205}Tl just prior to the excursion (Fig. 2) indicate a near-depletion of these depositional environments. The enlarged dissolved Mn pool would have permitted increased precipitation of Mn oxides during the brief oxygenation event associated with the EPME (Fig. 3c). Due to the short residence time of seawater Tl and its high sensitivity to changes in Mn oxide fluxes, this scenario can account for the brief perturbation in the ε^{205}Tl record at the EPME (Extended Data Fig. 2), especially if average global ocean redox conditions corresponded to the Mn reduction zone at the time.

Strong constraints exist on the range of viable mechanisms for generating a Mn oxide burial event during the EPME, especially given its short timescale. One potential way to drive increased Mn oxide burial is through a major sea-level transgression that expanded the area of oxic seafloor through flooding of continental shelves[45]. A sea-level rise is inferred to have occurred during the EPME interval, but the magnitude of the rise was modest compared to similar sea-level changes across the Late Permian[45,46]. Importantly, given the short transient nature of this oxygenation event, sea-level transgression is unlikely to be the controlling mechanism of Mn oxide burial fluxes, although it may have played a role.

An alternative cause is climatic cooling. Although a large negative excursion in oxygen isotope records documents hyperwarming during the EPME interval[9–13,22], this event was preceded by a small positive oxygen isotope excursion at the start of the EPME[10,12,13], suggesting the possibility of a brief cooling event concurrent with the short-term negative Tl isotope perturbation in our records (Fig. 4). Cooling could have enhanced Mn oxide burial through invigoration of thermohaline circulation via a steepened meridional temperature gradient and/or increased oxygen solubility in seawater[9], driving oxygenated waters into O_2-depleted regions of the global ocean. Whereas the long-term warming trend has been linked to massive CO_2 outgassing during LIP emplacement[5], co-emitted volcanogenic SO_2 could have triggered an initial brief cooling episode[7,9]. The massive release of volcanogenic SO_2 by the Siberian Traps LIP has been predicted based on both general effects of explosive volcanism and documented magmatic intrusions into the West Siberian Coal Field[5,9].

Modelling indicates that a Tl isotopic excursion of ~60–80 kyr duration could have been caused by a short-term oxygenation event (~5–20 kyr) induced by sulfate aerosol cooling, given an expected delayed response in oceanic circulation and gas solubility[9] and extended renewal time of a reservoir following a rapid isotopic excursion (see Supplementary Discussion, Extended Data Fig. 2 and Supplementary Data). Therefore, the Tl isotope records are

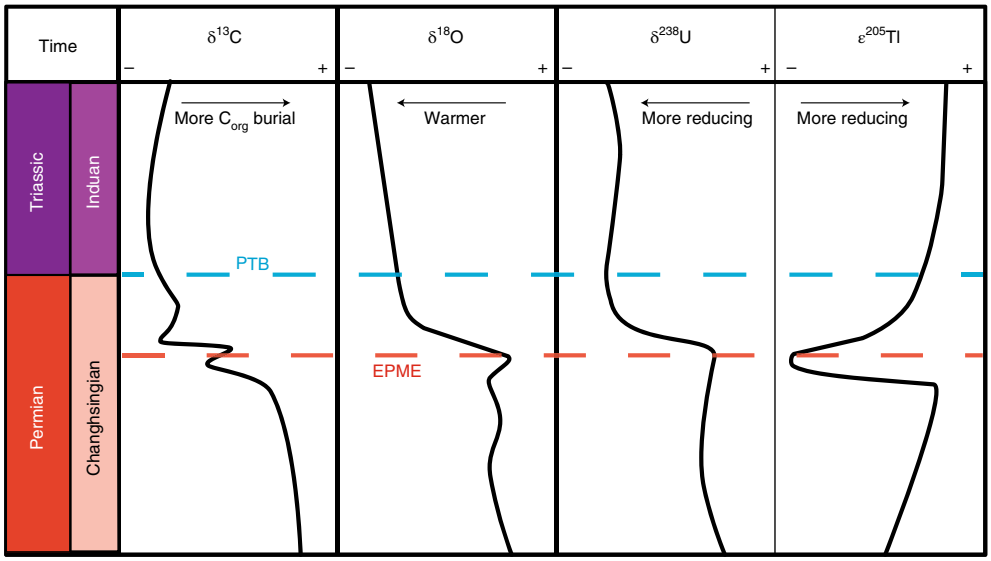

Fig. 4 | Generalized chemostratigraphic records of the Permian–Triassic transition. Compiled geochemical data include $\delta^{13}C$ (refs. [10–12,21,23–25,40,44,47,48]), $\delta^{18}O$ (refs. [10–13]), $\delta^{238}U$ (refs. [21,29]) and the $\varepsilon^{205}Tl$ record of this study. There is clear evidence of $\varepsilon^{205}Tl$ transitioning towards more anoxic (positive) values before the massive anoxic (negative) shift seen in the $\delta^{238}U$ record, indicating that the redox changes influencing Mn oxide burial rates (as recorded by Tl isotopes) occurred earlier than those influencing other redox-sensitive proxies. The large negative $\varepsilon^{205}Tl$ excursion, representing a rapid and short-lived oxygenation event, was approximately correlative with a minor positive $\delta^{18}O$ excursion[10–12] and negative $\delta^{13}C$ excursion[10,47,48], potentially recording a transient cooling linked to volcanogenic sulfate emissions.

consistent with the hypothesis of short-term climatic cooling and oceanic oxygenation at the onset of the EPME. This hypothesis is further supported by a small negative $\delta^{13}C$ excursion at the beginning of the EPME[10,47,48], due to either enhanced remineralization of organic carbon or release of ^{13}C-depleted volcanic CO_2.

Following the negative Tl isotope excursion at the EPME, all three study sections exhibit a shift towards more positive values, indicating a return to widespread anoxic conditions that persisted well into the earliest Triassic (Fig. 3d), a redox pattern that is corroborated by $\delta^{238}U$ studies[21,29]. Hyperwarming has been postulated as the cause for highly stratified and anoxic Early Triassic oceans[11,21,24]. This climatic warming and induced global anoxia following the EPME would have contributed to the protracted Early Triassic recovery[5,11,24,27].

Our $\varepsilon^{205}Tl$ record suggests a more complex redox history during the EPME than previously inferred. These perturbations in global climate[10–13] and oceanic redox state indicate that the EPME was induced not merely by a transition to more anoxic seawater but, rather, by rapid redox fluctuations coupled with substantial temperature variations[9,10,12,13,22]. Collectively, these stresses affected many marine clades[6,15,43], including those adapted to the more reducing conditions that preceded the EPME[49]. The persistence of widespread seafloor anoxia through part of the Early Triassic, as indicated by previous Permian–Triassic $\delta^{238}U$ studies[21,29] and confirmed by this $\varepsilon^{205}Tl$ record, was likely a factor in the protracted post-EPME recovery interval[5,11,24,27].

Online content

Any methods, additional references, Nature Research reporting summaries, source data, extended data, supplementary information, acknowledgements, peer review information; details of author contributions and competing interests; and statements of data and code availability are available at https://doi.org/10.1038/s41561-021-00802-4.

Received: 29 June 2020; Accepted: 13 May 2021;
Published online: 02 August 2021

References

1. Raup, D. M. Size of the Permo-Triassic bottleneck and its evolutionary implications. *Science* **206**, 217–218 (1979).
2. Sepkoski, J. J.Jr Ten years in the library: new data confirm paleontological patterns. *Paleobiology* **19**, 43–51 (1993).
3. Fan, J. et al. A high-resolution summary of Cambrian to early Triassic marine invertebrate biodiversity. *Science* **367**, 272–277 (2020).
4. Erwin, D. H. The Permo–Triassic extinction. *Nature* **367**, 231–236 (1994).
5. Burgess, S. D., Muirhead, J. D. & Bowring, S. A. Initial pulse of Siberian Traps sills as the trigger of the end-Permian mass extinction. *Nat. Commun.* **8**, 164 (2017).
6. Bond, D. P. G. & Grasby, S. E. On the causes of mass extinctions. *Palaeogeogr. Palaeoclimatol. Palaeoecol.* **478**, 3–29 (2017).
7. Broadley, M. W., Barry, P. H., Ballentine, C. J., Taylor, L. A. & Burgess, R. End-Permian extinction amplified by plume-induced release of recycled lithospheric volatiles. *Nat. Geosci.* **11**, 682–687 (2018).
8. Benton, M. J. Hyperthermal-driven mass extinctions: killing models during the Permian–Triassic mass extinction. *Philos. Trans. R. Soc. A* **376**, 20170076 (2018).
9. Black, B. A. et al. Systemic swings in end-Permian climate from Siberian Traps carbon and sulfur outgassing. *Nat. Geosci.* **11**, 949–954 (2018).
10. Shen, S.-Z. et al. End-Permian mass extinction and palaeoenvironmental changes in Neotethys: evidence from an oceanic carbonate section in southwestern Tibet. *Glob. Planet. Change* **73**, 3–14 (2010).
11. Sun, Y. et al. Lethally hot temperatures during the Early Triassic greenhouse. *Science* **338**, 366–370 (2012).
12. Chen, J. et al. High-resolution SIMS oxygen isotope analysis on conodont apatite from South China and implications for the end-Permian mass extinction. *Palaeogeogr. Palaeoclimatol. Palaeoecol.* **448**, 26–38 (2016).
13. Joachimski, M. M., Alekseev, A. S., Grigoryan, A. & Gatovsky, Y. A. Siberian Trap volcanism, global warming and the Permian-Triassic mass extinction: new insights from Armenian Permian-Triassic sections. *Geol. Soc. Am. Bull.* **132**, 427–443 (2020).
14. Hinojosa, J. L. et al. Evidence for end-Permian ocean acidification from calcium isotopes in biogenic apatite. *Geology* **40**, 743–746 (2012).
15. Grasby, S. E. et al. Progressive environmental deterioration in northwestern Pangea leading to the latest Permian extinction. *Geol. Soc. Am. Bull.* **127**, 1331–1347 (2015).
16. Sephton, M. A., Jiao, D., Engel, M. H., Looy, C. V. & Visscher, H. Terrestrial acidification during the end-Permian biosphere crisis? *Geology* **43**, 159–162 (2015).
17. Bond, D. P. G. & Wignall, P. B. Pyrite framboid study of marine Permian–Triassic boundary sections: a complex anoxic event and its relationship to contemporaneous mass extinction. *Geol. Soc. Am. Bull.* **122**, 1265–1279 (2010).

18. Algeo, T. J. et al. Spatial variation in sediment fluxes, redox conditions, and productivity in the Permian–Triassic Panthalassic Ocean. *Palaeogeogr. Palaeoclimatol. Palaeoecol.* **308**, 65–83 (2011).
19. Schoepfer, S. D. et al. Termination of a continent-margin upwelling system at the Permian–Triassic boundary (Opal Creek, Alberta, Canada). *Glob. Planet. Change* **105**, 21–35 (2013).
20. Mettam, C. et al. High-frequency fluctuations in redox conditions during the latest Permian mass extinction. *Palaeogeogr. Palaeoclimatol. Palaeoecol.* **485**, 210–223 (2017).
21. Zhang, F. et al. Congruent Permian-Triassic $\delta^{238}U$ records at Panthalassic and Tethyan sites: confirmation of global-oceanic anoxia and validation of the U-isotope paleoredox proxy. *Geology* **46**, 327–330 (2018).
22. Penn, J. L., Deutsch, C., Payne, J. L. & Sperling, E. A. Temperature-dependent hypoxia explains biogeography and severity of end-Permian marine mass extinction. *Science* **362**, eaat1327 (2018).
23. Grice, K. et al. Photic zone euxinia during the Permian–Triassic superanoxic event. *Science* **307**, 706–709 (2005).
24. Song, H. et al. Early Triassic seawater sulfate drawdown. *Geochim. Cosmochim. Acta* **128**, 95–113 (2014).
25. Grasby, S. E., Beauchamp, B., Bond, D. P. G., Wignall, P. B. & Sanei, H. Mercury anomalies associated with three extinction events (Capitanian Crisis, Latest Permian Extinction and the Smithian/Spathian Extinction) in NW Pangea. *Geol. Mag.* **153**, 285–297 (2016).
26. Visscher, H. et al. Environmental mutagenesis during the end-Permian ecological crisis. *Proc. Natl Acad. Sci. USA* **101**, 12952–12956 (2004).
27. Algeo, T. J. & Twitchett, R. J. Anomalous Early Triassic sediment fluxes due to elevated weathering rates and their biological consequences. *Geology* **38**, 1023–1026 (2010).
28. Algeo, T. J., Chen, Z. Q., Fraiser, M. L. & Twitchett, R. J. Terrestrial–marine teleconnections in the collapse and rebuilding of Early Triassic marine ecosystems. *Palaeogeogr. Palaeoclimatol. Palaeoecol.* **308**, 1–11 (2011).
29. Lau, K. V., Romaniello, S. J. & Zhang, F. in *Elements in Geochemical Tracers in Earth System Science* https://doi.org/10.1017/9781108584142 (Cambridge Univ. Press, 2019).
30. Kendall, B., Dahl, T. W. & Anbar, A. D. The stable isotope geochemistry of molybdenum. *Rev. Mineral. Geochem.* **82**, 683–732 (2017).
31. Owens, J. D., Nielsen, S. G., Horner, T. J., Ostrander, C. M. & Peterson, L. C. Thallium-isotopic compositions of euxinic sediments as a proxy for global manganese-oxide burial. *Geochim. Cosmochim. Acta* **213**, 291–307 (2017).
32. Owens, J. D. *in Elements in Geochemical Tracers in Earth System Science* https://doi.org/10.1017/9781108688697 (Cambridge Univ. Press, 2019).
33. Ostrander, C. M., Owens, J. D. & Nielsen, S. G. Constraining the rate of oceanic deoxygenation leading up to a Cretaceous Oceanic Anoxic Event (OAE-2: ~94 Ma). *Sci. Adv.* **3**, e1701020 (2017).
34. Them, T. R. et al. Thallium isotopes reveal protracted anoxia during the Toarcian (Early Jurassic) associated with volcanism, carbon burial, and mass extinction. *Proc. Natl Acad. Sci. USA* **115**, 6596–6601 (2018).
35. Bowman, C. N. et al. Linking the progressive expansion of reducing conditions to a stepwise mass extinction event in the late Silurian oceans. *Geology* **47**, 968–972 (2019).
36. Rue, E. L., Smith, G. J., Cutter, G. A. & Bruland, K. W. The response of trace-element redox couples to suboxic conditions in the water column. *Deep Sea Res. I* **44**, 113–134 (1997).
37. Nielsen, S. G., Rehkämper, M. & Prytulak, J. Investigation and application of thallium isotope fractionation. *Rev. Mineral. Geochem.* **82**, 759–798 (2017).
38. Fan, H. et al. Constraining oceanic oxygenation during the Shuram excursion in South China using thallium isotopes. *Geobiology* **18**, 348–365 (2020).
39. Kaiho, K. et al. Changes in depth-transect redox conditions spanning the end-Permian mass extinction and their impact on the marine extinction: evidence from biomarkers and sulfur isotopes. *Glob. Planet. Change* **94–95**, 20–32 (2012).
40. Schoepfer, S. D., Henderson, C. M., Garrison, G. H. & Ward, P. D. Cessation of a productive coastal upwelling system in the Panthalassic Ocean at the Permian–Triassic Boundary. *Palaeogeogr. Palaeoclimatol. Palaeoecol.* **313–314**, 181–188 (2012).
41. Nielsen, S. G., Rehkämper, M., Baker, J. & Halliday, A. N. The precise and accurate determination of thallium isotope compositions and concentrations for water samples by MC-ICPMS. *Chem. Geol.* **204**, 109–124 (2004).
42. Rehkämper, M. et al. Thallium isotope variations in seawater and hydrogenetic, diagenetic, and hydrothermal ferromanganese deposits. *Earth Planet. Sci. Lett.* **197**, 65–81 (2002).
43. Kiessling, W. et al. Pre-mass extinction decline of latest Permian ammonoids. *Geology* **46**, 283–286 (2018).
44. Payne, J. L. & Clapham, M. E. End-Permian mass extinction in the oceans: an ancient analog for the twenty-first century? *Annu. Rev. Earth Planet. Sci.* **40**, 89–111 (2012).
45. Shen, S.-Z. et al. A sudden end-Permian mass extinction in South China. *Geol. Soc. Am. Bull.* **131**, 205–223 (2019).
46. Haq, B. U. & Schutter, S. R. A chronology of Paleozoic sea-level changes. *Science* **322**, 64–68 (2008).
47. Clarkson, M. O. et al. A new high-resolution $\delta^{13}C$ record for the Early Triassic: insights from the Arabian Platform. *Gondwana Res.* **24**, 233–242 (2013).
48. Korte, C. & Kozur, H. W. Carbon-isotope stratigraphy across the Permian–Triassic boundary: a review. *J. Asian Earth Sci.* **39**, 215–235 (2010).
49. Fenchel, T. & Finlay, B. J. Oxygen toxicity, respiration and behavioural responses to oxygen in free-living anaerobic ciliates. *J. Gen. Microbiol.* **136**, 1953–1959 (1990).
50. Blakey, R. C. Triassic global paleogeographic map. *Global Paleogeography and Tectonics in Deep Time Series* (Deep Time Maps Inc., 2016); https://deeptimemaps.com/global-paleogeography-and-tectonics-in-deep-time/

Methods

Thallium isotope analysis. Powdered shale samples were dissolved using techniques modified from previous studies[31–33,37,51]. Samples were dissolved in 2 M HNO_3 at 130 °C for 12 h to separate the leachable material that contains the Tl adsorbed to pyrite, followed by digestion of the leached fraction in concentrated HNO_3-HCl to dissolve all organic compounds. After sample digestion, the Tl was purified through previously established column chemistry methods using micro-columns filled with Bio-Rad AG 1-X8 anion exchange resin to remove all Pb from samples[33,41,51,52]. NIST-SRM-981 Pb was then added as a spike to the Tl samples to track mass bias during mass spectrometry analysis[51]. The samples were then run on a Neptune multicollector inductively coupled plasma mass spectrometer using an Aridus II autosampler at the National High Magnetic Field Laboratory in the Geochemistry group for Tl isotopic composition[51]. Comparison to the United States Geological Survey shale reference material SCo-1, which has a long-term precision of $\varepsilon^{205}Tl = -3.0 \pm 0.3$ (2σ) (refs. [31–33]), was made to assess the precision of the entire method. A total of 80 samples were analysed, with 71 samples being selected here and for the supplementary information based on having an uncertainty of less than 0.5 (2σ, based on two or more replicate analyses). All samples that had 2σ values below the analytical uncertainty of 0.3 had the error bars increased to 0.3 as this is the error for the geostandard from the entire method.

Organic carbon isotope analysis. Organic carbon isotopes for Gujo-Hachiman and Ubara were determined using the same methods as in previous studies[35,40], whereas carbon isotopes had already been determined for Opal Creek[19]. Powdered samples were decarbonated using 6 M HCl until effervescence ceased (typically ~1 min due to low carbonate content), rinsed three times with deionized water (18 MΩ), dried and homogenized. Samples were then weighed out into tin cups and measured on a Thermo Finnigan DELTAplus XP stable isotope ratio mass spectrometer using a Carlo Erba Elemental Analyser, and results were compared to those of external lab standard acetanilide (−29.2‰) and Florida State University in-house standards urea-2 (−8.13‰), and Y1 sugar (−12.7‰) with uncertainties of ± 0.2‰ for all (ref. [35]) at the National High Magnetic Field Laboratory in the Geochemistry group.

Data availability

The datasets generated during the current study are available as supplementary files alongside the published manuscript. They are available through the Pangaea online data repository at https://doi.pangaea.de/10.1594/PANGAEA.933389.

References

51. Nielsen, S. G. et al. Thallium isotope composition of the upper continental crust and rivers—an investigation of the continental sources of dissolved marine thallium. *Geochim. Cosmochim. Acta* **69**, 2007–2019 (2005).
52. Baker, R. G. A., Rehkämper, M., Hinkley, T. K., Nielsen, S. G. & Toutain, J. P. Investigation of thallium fluxes from subaerial volcanism—implications for the present and past mass balance of thallium in the oceans. *Geochim. Cosmochim. Acta* **73**, 6340–6359 (2009).
53. Burgess, S. D., Bowring, S. & Shen, S.-Z. High-precision timeline for Earth's most severe extinction. *Proc. Natl Acad. Sci. USA* **111**, 3316–3321 (2014).

Acknowledgements

We thank C. Bowman, N. Kozik and A. Karl for assistance in sample processing and data collection. The FSU EOAS Winchester Fund helped fund work done by S.M.N. Grants to J.D.O. through the NASA Exobiology program (NNX16AJ60G and 80NSSC18K1532) and the Sloan Research Foundation (FG-2020–13552) funded this work. This work was performed at the National High Magnetic Field Laboratory in Tallahassee, Florida, which is supported by National Science Foundation Cooperative Agreement No. DMR-1644779 and by the State of Florida.

Author contributions

S.M.N. processed the samples and performed Tl isotope analyses with contributions and direction from J.D.O. S.M.N. and J.D.O. developed the project idea and discussed and analysed the data. S.D.S. and T.J.A. provided samples. S.M.N. wrote the manuscript with direction from J.D.O. and contributions from all co-authors.

Competing interests

The authors declare no competing interests.

Additional information

Extended data is available for this paper at https://doi.org/10.1038/s41561-021-00802-4.

Supplementary information The online version contains supplementary material available at https://doi.org/10.1038/s41561-021-00802-4.

Correspondence and requests for materials should be addressed to S.M.N.

Peer review information *Nature Geoscience* thanks Matthew Clarkson and the other, anonymous, reviewer(s) for their contribution to the peer review of this work.

Reprints and permissions information is available at www.nature.com/reprints.

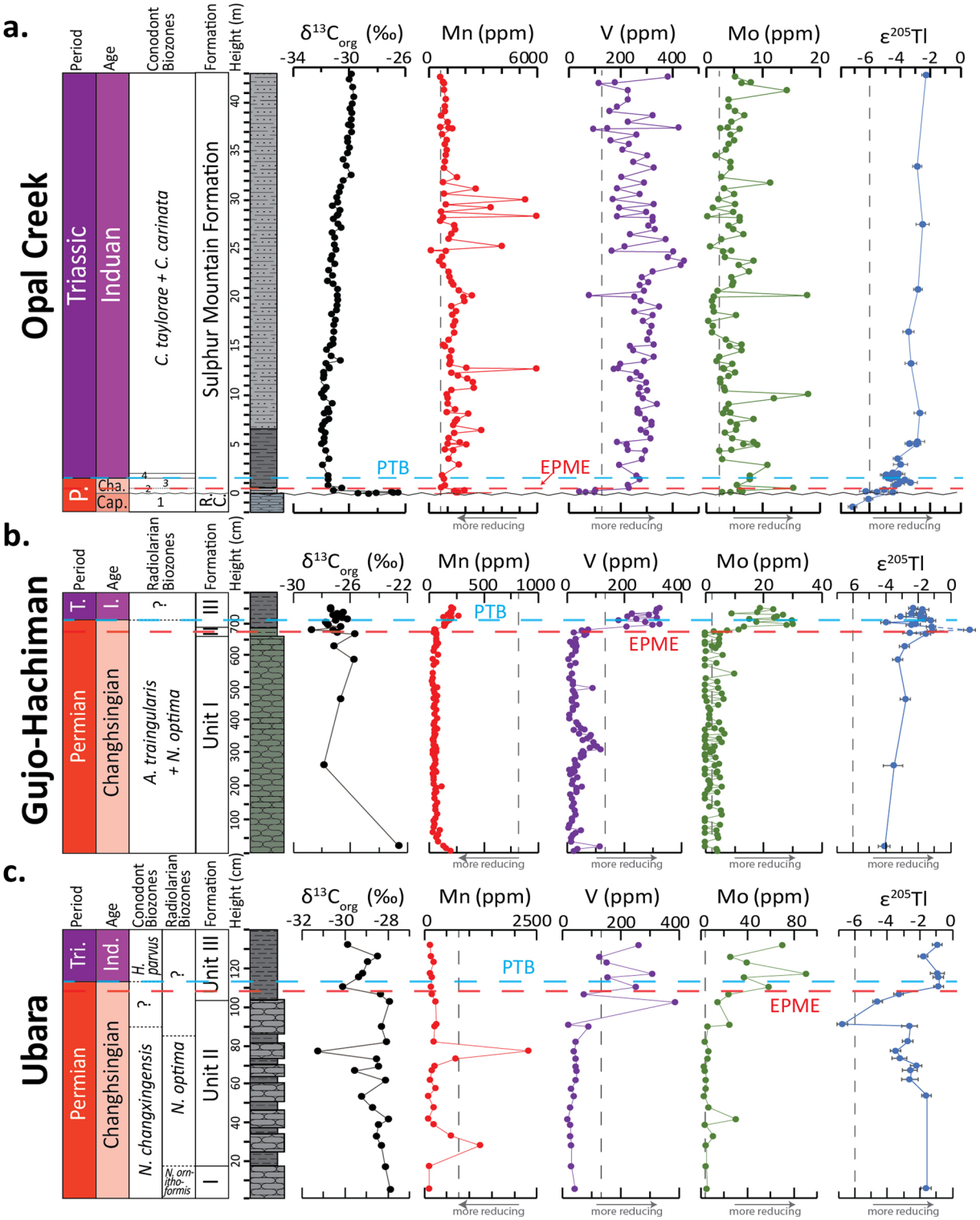

Extended Data Fig. 1 | See next page for caption.

Extended Data Fig. 1 | Full chemostratigraphy of all three sections. Biostratigraphy, lithostratigraphy, and chemostratigraphy for Opal Creek (**a**), Gujo-Hachiman (**b**), and Ubara (**c**). Chemostratigraphy includes carbon isotopes (black line), manganese concentrations (red line), vanadium concentrations (purple line), molybdenum concentrations (green line), and thallium isotopes (blue line). Biostratigraphy, lithostratigraphy, and trace metal concentrations are from previous sources[18,19,39,40], as well as carbon isotopes of Opal Creek[40]. For Opal Creek, biozones 1–4 represent *Mesogondolella bitteri* and *M. rosenckrantzi* (1), *M. sheni* (2), *Clarkina hauschkei* and *C. meishanensis* (3), and *Hindeodus parvus* (4). Lithostratigraphic columns are present on the left adjacent to height. Separate patterns are used to distinguish lithologies, including chert (rounded bricks), shale (dashed lines), and silty mudstones (dashed and dotted lines), with approximate colour of the rocks. All three trace metal concentration charts have upper continental crust concentrations marked with a dashed vertical line, with arrow pointing towards more reducing conditions. The Tl isotope plots have a dashed vertical line indicating modern seawater values, with more positive values representing greater extent of anoxia. All three sites are correlated with the EPME (red dashed line) and PTB (light blue dashed line) using both biostratigraphy and carbon isotope stratigraphy. Thallium plotted with error bars (2σ). Opal Creek features an Upper Permian[19,40] unconformity near the base of the described section (wavy line), below the EPME. Opal Creek here features a more extensive section up to 43m as compared to Fig. 2. Trace metal concentrations generally indicate reducing conditions at all three sections, though each trace metal responds in a different manner for each locality due to fluctuating local redox[18,19]. Global similarity in thallium isotopes despite this indicates little local explanation for the excursion.

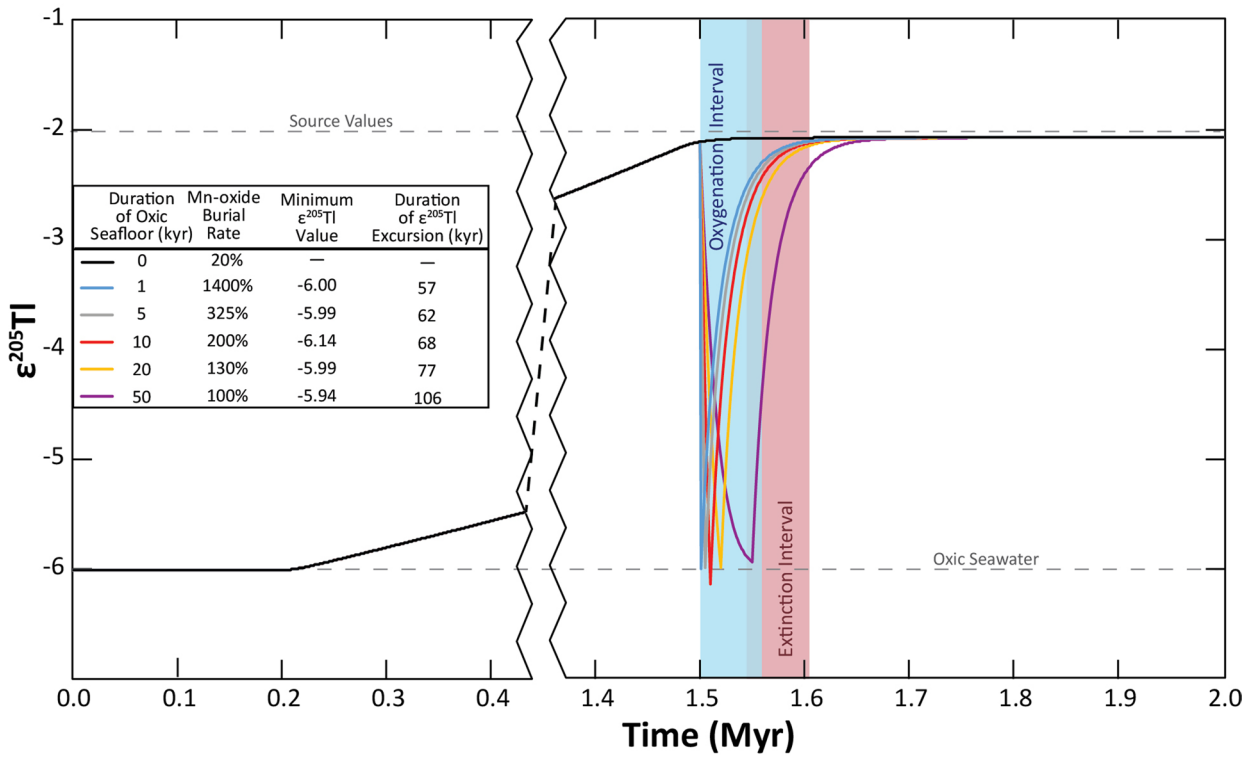

Extended Data Fig. 2 | Modeled Tl isotopic values across the EPME. Model showing how changes in Mn oxide burial can cause the negative isotope excursion exhibited during the EPME. Parameters can be found in Extended Data Table 1. The approximate duration of the oxygenation interval (~60 kyr;[18] see Supplementary Discussion) is highlighted in blue, while the approximate duration of the extinction interval (~60 kyr[53]) is highlighted in red, with these slightly overlapping based on average position of the negative thallium isotope excursion compared to the negative carbon isotope excursion (see Fig. 4). Various runs were conducted under the premise of decreasing Mn oxide burial between 0.20 and 1.50 Myr, representing the upper Changhsingian data found in the lower part of the Gujo-Hachiman section. As there is relatively small change at a steady rate across this interval, a gap between 0.4 and 1.4 Myr was applied for convenience of space, though this trend continues at a constant rate across this interval (represented as a dashed line in the gap). Following this, a short-term major increase in Mn oxide burial is recreated. The duration and flux of Mn oxide burial is modulated so that the minimum value of the excursion is consistent, all values near $\varepsilon^{205}Tl = \sim -6.0$, with included table within the figure to distinguish the different runs and how the duration of the excursion compares. This can be compared to a scenario with no major isotope excursion (thick black line).